

Direct Gibbs Ensemble Monte Carlo Simulations for Solid–Vapor Phase Equilibria: Applications to Lennard–Jonesium and Carbon Dioxide

Bin Chen,^{†,‡} J. Ilja Siepmann,^{*,†} and Michael L. Klein[‡]

Department of Chemistry and Department of Chemical Engineering and Materials Science, University of Minnesota, 207 Pleasant Street SE, Minneapolis, Minnesota 55455-0431, Laboratory for Research on the Structure of Matter and Center for Molecular Modeling, University of Pennsylvania, 3231 Walnut Street, Philadelphia, Pennsylvania 19104-6202

Received: May 22, 2001; In Final Form: July 2, 2001

The Gibbs ensemble Monte Carlo method of Panagiotopoulos is extended to calculations of solid–vapor coexistence curves. As in the original Gibbs ensemble method, the new technique makes use of two simulation boxes that are in thermodynamic contact. However, the box that contains the solid phase is elongated along one axis and contains only a slab of solid material surrounded on both sides by vapor. Aggregation-volume-bias Monte Carlo moves are used to sample transfers from the solid to the vapor and vice versa in this box, whereas the usual particle swap moves are applied to transfers between the solid–vapor box and the other box that contains a bulk vapor phase. Volume moves for the solid–vapor box use separate displacements of individual cell lengths or of individual **H**-matrix elements. As one approaches the triple-point temperature from below, increased disorder at the solid–vapor interface is observed, and once the triple-point temperature is exceeded, the entire solid slab converts to a liquid. The use of configurational-bias Monte Carlo particle swap moves enables us to extend conventional Gibbs ensemble simulations of vapor–liquid equilibria beyond the triple point into the supercooled regime. Clausius–Clapeyron fits to the sublimation, and vapor pressure curves allow for the precise determination of the triple-point location. The simulation results for Lennard–Jonesium are in excellent agreement with Gibbs–Duhem integration simulations, and the results for carbon dioxide using the TraPPE force field reproduce well the experimental data (e.g., the predicted triple-point parameters are $T = 212 \pm 2$ K and $p = 430 \pm 50$ kPa).

1. Introduction

Solid–fluid phase equilibria are of great importance in many biological, geological, environmental, and technological processes. The seminal development of the Gibbs ensemble Monte Carlo method^{1–3} in the late 1980s has made the calculation of fluid phase equilibria a relatively routine task for molecular simulation.^{4–6} In particular, the Gibbs ensemble method allows the direct calculation of mixture equilibria for arbitrary numbers of components and fluid phases.^{7,8} Particle swap moves are employed in conventional Gibbs ensemble simulations to establish chemical potential equilibrium between the fluid phases. However, particle insertions and removals of single particles fail for crystalline phases because they involve the creation of interstitial or vacancy defects. The crystalline symmetry would allow for the insertion/removal of entire layers, but these multi-particle moves are plagued by extremely low acceptance rates. Therefore, molecular simulation studies of solid–fluid equilibria are most often carried out with the Einstein crystal method,^{9–11} which makes use of thermodynamic integrations starting from an Einstein crystal for the solid phase and from an ideal gas for the fluid phase to find a state point with equal free energy for both phases. Thus, multiple simulations are required to find one coexistence point, and in particular, for flexible molecules these calculations require elaborate procedures.^{12–15} Although it should be noted here that once the

first point on a solid–fluid coexistence line has been determined via the Einstein method, the Gibbs–Duhem integration technique can be used to trace the coexistence line in a relatively straightforward manner.^{15–18} Another approach to the calculation of solid–fluid equilibria is based on the cell model,^{19–21} but is less often used than the Einstein method.

In this work, we demonstrate that an extension of the Gibbs ensemble Monte Carlo method^{1–3} combined with the configurational-bias^{22–24} and aggregation-volume-bias^{25,26} Monte Carlo sampling schemes allows one to carry out direct simulations of solid–vapor equilibria. As in the conventional Gibbs ensemble method, the new approach makes use of multiple simulation boxes that are in thermodynamic contact. However, the box that contains the solid phase is elongated along one axis and contains only a slab of solid material surrounded on both sides by vapor. A single simulation box with a liquid-phase slab surrounded by vapor has been previously used to investigate vapor–liquid phase equilibria via direct molecular dynamics simulations.^{27–29} The solid–vapor Gibbs ensemble Monte Carlo method is presented in the next section. This extended algorithm is applied here to the calculation of the solid–vapor equilibria for Lennard–Jonesium and carbon dioxide (a molecule with an unusually high ratio of triple point and critical point temperatures). In section 3, the molecular models and simulation details of this study are briefly described. The results of the simulations for Lennard–Jonesium and carbon dioxide are presented and discussed in section 4, and section 5 provides concluding remarks.

* Corresponding author. E-mail: siepmann@chem.umn.edu.

[†] University of Minnesota.

[‡] University of Pennsylvania.

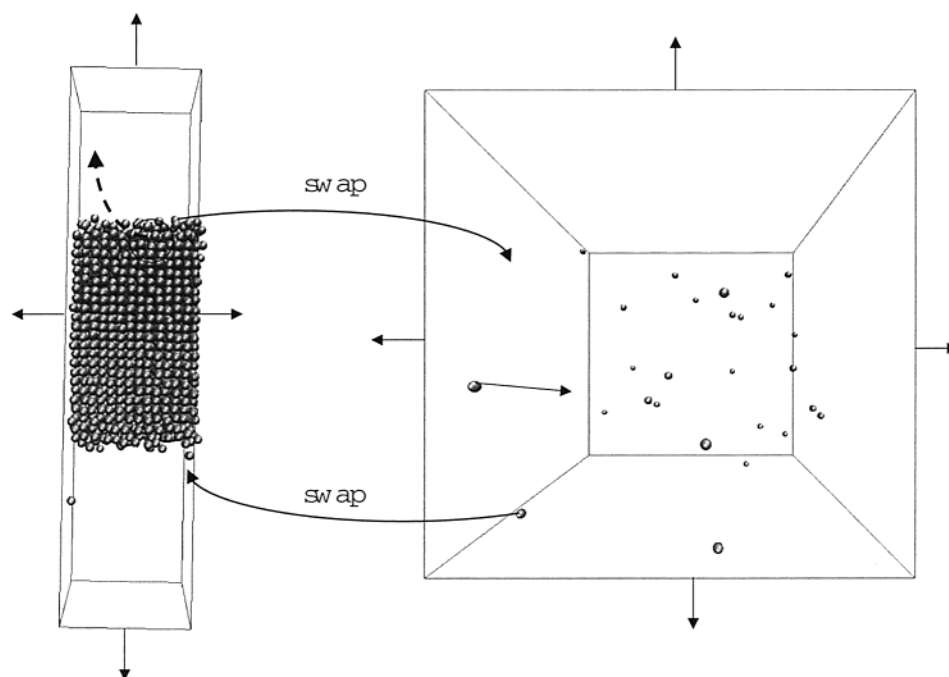


Figure 1. Setup of the Gibbs ensemble Monte Carlo method for solid–vapor phase equilibria. The elongated box on the left contains a solid slab surrounded by vapor, while the cubic box on the right contains a bulk vapor phase.

2. Solid–Vapor Gibbs Ensemble Monte Carlo Method

The solid–vapor Gibbs ensemble Monte Carlo method is described here in its canonical ensemble variant suitable for simulations of one-component solid–vapor equilibria. However, the obvious modifications to an isobaric–isothermal setup² or to more than two simulation boxes⁷ allow for simulations of multicomponent systems and solid–liquid–vapor or solid–solid–vapor equilibria.

Figure 1 shows the general set-up of the solid–vapor Gibbs ensemble Monte Carlo method. As mentioned in the Introduction, direct particle insertions or removals fail for crystalline phases. In contrast, molecular simulations have been used to investigate melting or freezing at solid–fluid interfaces.^{30,31} Thus, one might in principle use a direct simulation approach²⁹ with a solid-slab surrounded by vapor to study solid–vapor equilibria. However, at equilibrium, the rate of transfer between the two phases would be very low. Recently, we have introduced the aggregation-volume-bias Monte Carlo method^{25,26} for the efficient sampling of strongly associating fluids. Similar to the clusters found in associating fluids, particles in a crystalline environment possess a very favorable energy but pay an entropic penalty compared to vapor-phase molecules. The aggregation-volume-bias Monte Carlo method exploits the balance of enthalpy and entropy and greatly facilitates the transfer of particles between the solid and vapor regions of the solid-slab box. Once an equilibrium has been established in the solid-slab box, one might question why a separate vapor box should be added to the system. However, the separate vapor box offers two significant advantages. First, the pressure can be calculated very precisely for the vapor box, whereas the pressure fluctuations are much more significant in the solid-slab box. (For a similar reason, conventional Gibbs ensemble simulations usually report the pressure of the vapor phase and not that of the liquid phase.) Second, the usual single-particle Monte Carlo moves are very inefficient in sampling volume fluctuations of the solid slab. Thus, the addition of a separate vapor box allows one to carry out the usual volume swap moves between the vapor and

solid-slab box, thereby sampling the collective expansion/compression modes of the solid slab. In the case of a solid–vapor Gibbs ensemble simulation, it is also beneficial to independently sample the three cell lengths of the rectangular solid-slab box; i.e., whereas the volume move for the vapor-box is carried out with a uniform transformation, a random axis is picked for the solid-slab box, and only the coordinates of this axis are displaced.³² In addition, Rahman–Parrinello moves^{33,34} of individual elements of the **H**-matrix can also be used for the solid-slab box. Finally, the usual translational, rotational, and conformational (only for flexible molecules) moves complete the solid–vapor Gibbs ensemble Monte Carlo method. As in vapor–liquid Gibbs ensemble simulations, configurational-bias Monte Carlo moves^{22–24} are used to sample intramolecular conformations and to facilitate particle swaps between the two simulation boxes.

3. Molecular Models and Simulation Details

A. Lennard–Jonesium. Two series of simulations were carried out for Lennard–Jonesium. The solid-slab Gibbs ensemble method was used to determine the solid–vapor coexistence curve, while the conventional Gibbs ensemble set-up was used to calculate the vapor–liquid coexistence curve. Since use of a solid-slab setup precludes the straightforward use of analytical tail corrections,³⁵ all simulations were carried out for Lennard–Jonesium with a spherical potential truncation for separations greater than 4.75σ .

The solid–vapor simulations were started using a solid slab of $7 \times 7 \times 12$ unit cells ($N = 2352$) placed in a box of dimensions $11.2\sigma \times 11.2\sigma \times 40\sigma$. The initial length of the vapor box ranged from 26σ ($T^* = 0.687$) to 50σ ($T^* = 0.585$). The equilibration and production periods consisted of at least 2×10^4 and 2×10^5 Monte Carlo cycles, respectively (N moves = 1 cycle). The type of Monte Carlo move was selected at random according to the following probabilities: 0.9000 (translation), 0.0955 (aggregation-volume-bias), 0.0040 (interbox particle swap), and 0.0005 (volume exchange). Configurational-bias

TABLE 1: Thermodynamic Properties of Lennard–Jonesium at Its Triple Point (TP) and Vapor–Liquid (VL) and Solid–Vapor (SV) Coexistence Data near the Triple Point^a

		T^*	$p^* (\times 10^3)$	ρ_{solid}^*	ρ_{liquid}^*	$\rho_{\text{vapor}}^* (\times 10^3)$	U_{solid}^*	U_{liquid}^*	$U_{\text{vapor}}^* (\times 10^3)$
Agrawal and Kofke	TP	0.687 ₄	1.1	0.963	0.850	1.86			
this work	TP	0.689 ₉	1.29 ₂₂	0.955 ₅	0.844 ₄	1.9 ₃			
Agrawal and Kofke	VL	0.690	1.14		0.858	1.67		−6.237	−2.01
this work	VL	0.687	1.24 ₁		0.8448 ₂	1.82 ₃		−6.062 ₁	−2.29 ₂
Agrawal and Kofke	SV	0.687	1.15	0.9622		1.702	−7.269		−2.123
this work	SV	0.687	1.24 ₁	0.954 ₃		1.84 ₂	−7.125 ₁		−2.25 ₂

^a Subscripts denote the statistical uncertainties in the last digits.

Monte Carlo moves^{24,36} with multiple insertions^{37,38} ($n_{\text{choice}}^{\text{first}} = 10$) were used to enhance the acceptance rate for the particle swap moves.

The vapor–liquid simulations were carried out for $N = 1728$. The total volume of the system was adjusted to yield vapor phases with at least 10 particles. The equilibration and production periods consisted of 2×10^4 and 2×10^5 Monte Carlo cycles, respectively. The type of Monte Carlo move was selected at random according to the following probabilities: 0.9000 (translation), 0.0995 (interbox particle swap), and 0.0005 (volume exchange). Configurational-bias Monte Carlo moves with multiple insertions ($n_{\text{choice}}^{\text{first}} = 10$) were used to enhance the acceptance rate for the particle swap moves.

B. Carbon Dioxide. The calculations for carbon dioxide used the TraPPE (transferable potentials for phase equilibria) force field.³⁹ This is a three-site model with rigid, linear structure and a carbon–oxygen bond length of 1.16 Å. Lennard–Jones sites and partial charges are placed on the atomic positions, and the parameters are as follows: $\sigma_{\text{CC}} = 2.80$ Å; $\epsilon_{\text{CC}}/k_{\text{B}} = 27.0$ K; $q_{\text{C}} = +0.70$ e; $\sigma_{\text{OO}} = 3.05$ Å; $\epsilon_{\text{OO}}/k_{\text{B}} = 79.0$ K; and $q_{\text{O}} = +0.35$ e. Lorentz–Berthelot-combining rules are used to determine the parameters for unlike Lennard–Jones interactions.³⁵ For the simulations described here, a molecule-based potential truncation at carbon–carbon separations of 16 Å was used for both Lennard–Jones and Coulombic interactions. As for Lennard–Jonesium, two series of simulations were carried to determine the solid–vapor and vapor–liquid coexistence curves.

The solid–vapor simulations were started using a solid slab of $6 \times 6 \times 12$ unit cells ($N = 1728$) placed in a box of dimensions $35 \text{ Å} \times 35 \text{ Å} \times 120 \text{ Å}$. The initial length of the vapor box ranged from 60 Å ($T = 210$ K) to 120 Å ($T = 190$ K). The equilibration and production periods consisted of at least 2×10^4 and 5×10^4 Monte Carlo cycles, respectively. The type of Monte Carlo move was selected at random according to the following probabilities: 0.4750 (translation and rotation), 0.0496 (interbox particle swap), and 0.0004 (volume exchange). Configurational-bias Monte Carlo moves with multiple insertions of the first bead ($n_{\text{choice}}^{\text{first}} = 10$), and multiple orientations ($n_{\text{choice}} = 5$) were used to enhance the acceptance rates for the particle swap moves.

The vapor–liquid simulations were carried out for $N = 1728$. The total volume of the system was adjusted to yield vapor phases with at least 20 particles. The equilibration and production periods consisted of 2×10^4 and 5×10^5 Monte Carlo cycles, respectively. The type of Monte Carlo move was selected at random according to the following probabilities: 0.4400 ($T = 200$ K) to 0.4950 ($T = 250$ K) (translation and rotation), 0.1198 ($T = 200$ K) to 0.0098 ($T = 250$ K) (interbox particle swap), and 0.0002 (volume exchange). Configurational-bias Monte Carlo moves with multiple insertions of the first bead ($n_{\text{choice}}^{\text{first}} = 10$), and multiple orientations ($n_{\text{choice}} = 5$) were used to enhance the acceptance rates for the particle swap moves.

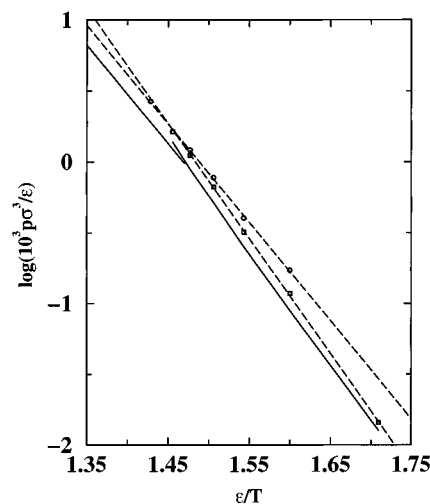


Figure 2. Clausius–Clapeyron plot of the sublimation and vaporization pressure curves for Lennard–Jonesium vs the inverse temperature. The solid lines are taken from the Gibbs–Duhem integration simulations by Agrawal and Kofke.¹⁷ The squares and circles represent the data from Gibbs ensemble simulations using the solid-slab or the conventional setup, respectively. Statistical errors in the pressure are smaller than the symbol size. The dashed lines depict weighted-linear least-squares fits to the sublimation and vapor pressure data obtained from the Gibbs ensemble simulations.

4. Results and Discussion

A. Lennard–Jonesium. Figure 2 shows the pressure–(inverse) temperature phase diagram of Lennard–Jonesium in the region close to the triple point. Both the sublimation and vaporization pressure lines can be fit well by straight lines as prescribed by the Clausius–Clapeyron equation,⁴⁰ and the triple point can be located by the intersection of these two lines. It should be noted here, that the use of configurational-bias Monte Carlo particle swap moves allows us to extend the conventional Gibbs ensemble simulations of Lennard–Jonesium to temperatures below the triple point; i.e., an equilibrium is established that involves a supercooled liquid phase. This supercooled liquid phase is stabilized by the cubic box used in the conventional Gibbs ensemble simulations, and nucleation of a crystalline phase was not observed. In contrast, when the solid-slab Gibbs ensemble simulations were extended beyond the triple point, we observed a surface-induced melting to a liquid slab (see below); i.e., the presence of the interface prevents the sampling of a superheated solid phase.

The thermodynamic properties of Lennard–Jonesium at its triple point are summarized in Table 1. The triple-point location determined from our simulations is $T^* = 0.689 \pm 0.009$ and $p^*/10^3 = 1.29 \pm 0.22$. In particular, the triple-point temperature is in excellent agreement with previous simulation estimates. However, the sublimation and vapor pressure curves and the triple-point pressure calculated in this work are shifted to higher pressures than those obtained by Agrawal and Kofke from

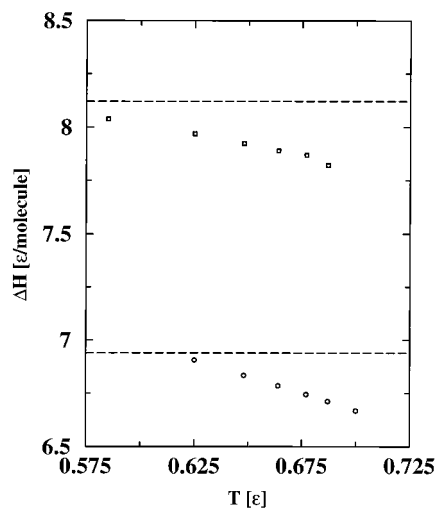


Figure 3. Heats of sublimation and vaporization for Lennard–Jonesium vs temperature. Squares and circles as in Figure 2. The dashed lines depict the values obtained from fits to the Clausius–Clapeyron equation (see Figure 2).

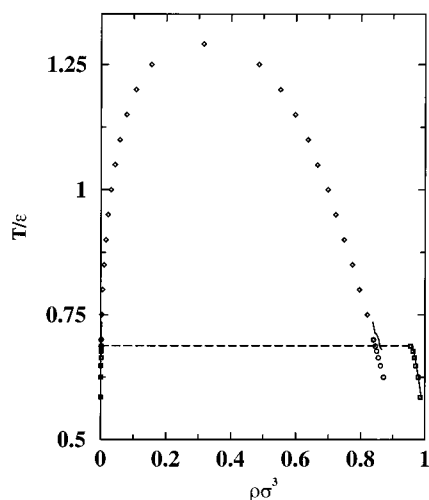


Figure 4. Temperature–density diagram for Lennard–Jonesium. Solid lines, squares, and circles as in Figure 2. The dashed line depicts the triple-point temperature from the Gibbs ensemble simulations. Diamonds show the results of histogram reweighting simulations in the grand canonical ensemble.⁴²

Gibbs–Duhem integrations.¹⁷ This discrepancy can be attributed to the different treatment of the long-range part of the potential (spherical cutoff at approximately 4σ with analytical long-range corrections used by Agrawal and Kofke¹⁷ versus a spherical truncation at 4.75σ without tail corrections used here). For the same reason, the internal energies of the liquid and solid phases⁴¹ obtained here are slightly smaller in magnitude than those of Agrawal and Kofke¹⁷ (see Table 1).

The heats of sublimation⁴¹ and of vaporization calculated directly from the Gibbs ensemble simulations and obtained from the Clausius–Clapeyron fits are compared in Figure 3. The increase in the heat of vaporization is very gradual with decreasing temperature and continues smoothly into the supercooled region. Close to the triple point ($T^* = 0.687$), the heat of sublimation is about 15% larger in magnitude than the heat of vaporization.

The temperature–density phase diagram of Lennard–Jonesium is shown in Figure 4. The orthobaric liquid and solid densities agree well with the Gibbs–Duhem results of Agrawal and Kofke.¹⁷ For comparison, the vapor–liquid coexistence

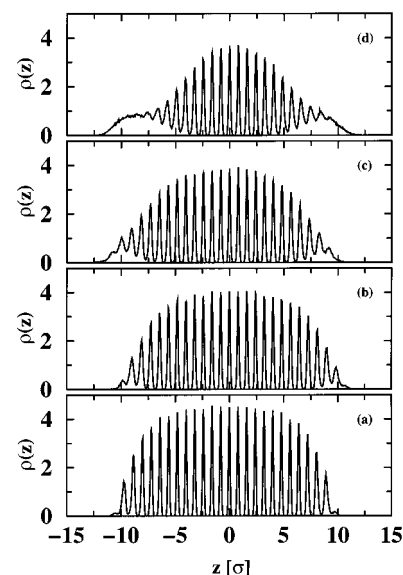


Figure 5. Density profiles for Lennard–Jonesium as a function of position along the z -axis. Results for the solid-slab setup are shown for $T^* = 0.585$ (part a), $T^* = 0.648$ (part b), $T^* = 0.677$ (part c), and $T^* = 0.687$ (part d).

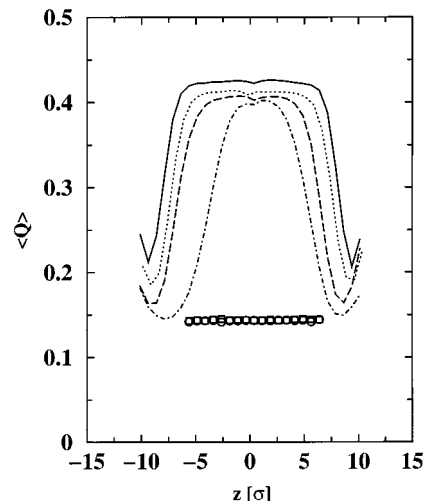


Figure 6. Translational order parameters (eq 1) for Lennard–Jonesium as a function of position along the z -axis. Results for the solid-slab setup (including all regions with density larger than $10^{-2}\rho_{\text{solid}}$) are shown for $T^* = 0.585$ (solid line), $T^* = 0.648$ (dotted), $T^* = 0.677$ (dashed), and $T^* = 0.687$ (dashed-dotted). Results for the bulk liquid are shown for $T^* = 0.648$ (squares) and $T^* = 0.687$ (circles).

curve calculated from histogram-reweighting Monte Carlo simulations in the grand canonical ensemble (using a cubic box with $L = 10\sigma$ and spherical potential truncations at 4.75σ) is also included.⁴² A mixed-field analysis of the histogram data⁴³ was used to estimate the critical parameters: $T_{\text{crit}}^* = 1.291$, $\rho_{\text{crit}}^* = 0.315$, and $p_{\text{crit}}^* = 0.120$. The ratios of the calculated triple-point over critical-point parameters ($T_{\text{triple}}/T_{\text{crit}} = 0.534$ and $p_{\text{triple}}/p_{\text{crit}} = 0.0108$) can be compared to experimental data for argon ($T_{\text{triple}}/T_{\text{crit}} = 0.556$ and $p_{\text{triple}}/p_{\text{crit}} = 0.0142$).⁴⁴ The good agreement demonstrates that Lennard–Jonesium is an adequate model for the three states of matter of argon.

As mentioned above, the solid-slab system undergoes a surface-induced melting transition as the triple-point temperature is exceeded. Density profiles of the solid slab systems are shown in Figure 5. At the lowest temperature ($T^* = 0.585$), the density profile approaches a step function with an interfacial width smaller than the interlayer spacing. Close to the triple point

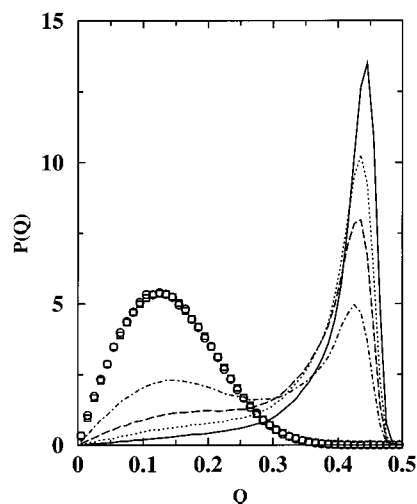


Figure 7. Distributions of translational order parameters (eq 1) for Lennard-Jonesium. Line styles and symbols as in Figure 6.

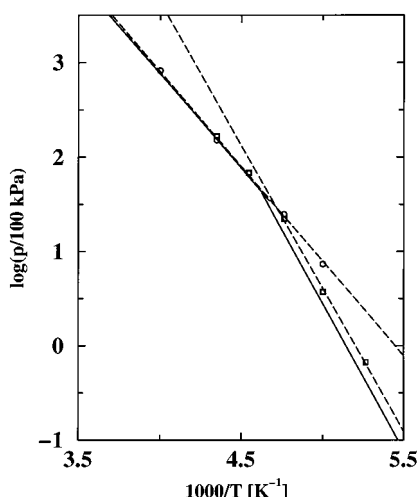


Figure 8. Clausius-Clapeyron plot of the sublimation and vaporization pressure curves for carbon dioxide vs the inverse temperature. The solid lines depict the experimental data.⁴⁷ The squares and circles represent the data from Gibbs ensemble simulations for the TraPPE force field using the solid-slab or the conventional setup, respectively. Statistical errors in the pressure are smaller than the symbol size. The dashed lines depict weighted-linear least-squares fits to the sublimation and vapor pressure data.

($T^* = 0.687$), it is possible to discern a central solid region with a mean density of 0.95 separated from a liquid-like outer region with a width of about 2σ and a mean density of about 0.85, i.e., close to the bulk liquid density obtained from the conventional Gibbs ensemble simulation at the same temperature.

Following Huitema et al.,³¹ one can define a translational order parameter, Q , as follows:

$$Q = \sqrt{\frac{4\pi}{13} \{ [\text{Re}(Q_{6-6}^a)]^2 + [\text{Re}(Q_{60}^a)]^2 + [\text{Re}(Q_{66}^a)]^2 \}} \quad (1)$$

where $\text{Re}(Q_{lm}^a)$ denotes the real part of Q_{lm}^a , which is given by

$$Q_{lm}^a = \frac{1}{N} \sum_{j=1}^N Y_{lm}[\theta(\mathbf{r}_{ij}), \phi(\mathbf{r}_{ij})] \quad (2)$$

where N is the number of nearest neighbors surrounding atom i , $Y_{lm}[\theta(\mathbf{r}_{ij}), \phi(\mathbf{r}_{ij})]$ is the spherical harmonic, and $\theta(\mathbf{r}_{ij})$ and $\phi(\mathbf{r}_{ij})$

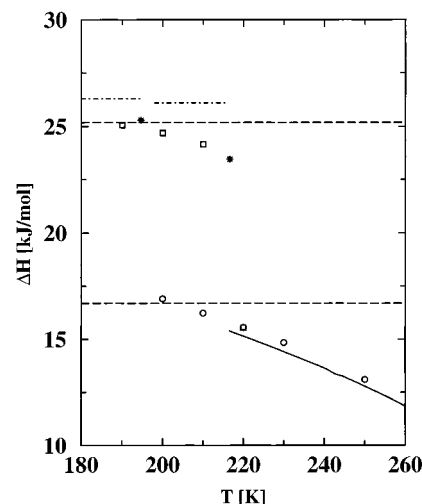


Figure 9. Heats of sublimation and vaporization for carbon dioxide vs temperature. Solid lines and stars depict the experimental data,^{46–48} and the dashed-dotted lines are taken from Antoine correlations;⁴⁷ squares, and circles as in Figure 8. The dashed lines depict the values obtained from fits to the Clausius-Clapeyron equation (see Figure 8).

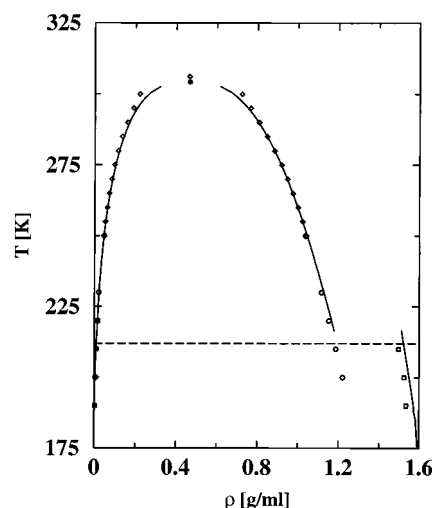


Figure 10. Temperature-density diagram for carbon dioxide. Solid lines,^{46–48} squares, and circles as in Figure 8. The dashed line depicts the triple-point temperature for the Gibbs ensemble simulations. Diamonds show the results of histogram reweighting simulations in the grand canonical ensemble.³⁹

are the polar and azimuthal angles of vector \mathbf{r}_{ij} (linking atom i to one of its nearest neighbors atom j) with respect to the reference z -axis. Following Huitema et al.,³¹ the fcc (111) axis was chosen as the reference z -axis. It has been shown by Huitema et al.³¹ that using this reference axis, the Q defined in eq 1 has a value of 0.48476 for an atom surrounded by nearest neighbors which are in a perfect fcc arrangement. The value of Q remains positive but decreases for low-symmetry structures, i.e., the fluids. The value of this order parameter is also dependent upon the reference axis. It should be noted that rotationally invariant order parameters have been used by van Duijneveldt and Frenkel.⁴⁵

The order parameters determined from the solid slab and the conventional Gibbs ensemble simulations are plotted as a function of z -position in Figure 6. At the lowest temperature ($T^* = 0.585$), the order parameter in the central region of the slab is close to the value of 0.48476 for a perfect fcc crystal, and the interfacial region is very sharp; i.e., crystalline order extends to all but the outermost layer of the slab. The small

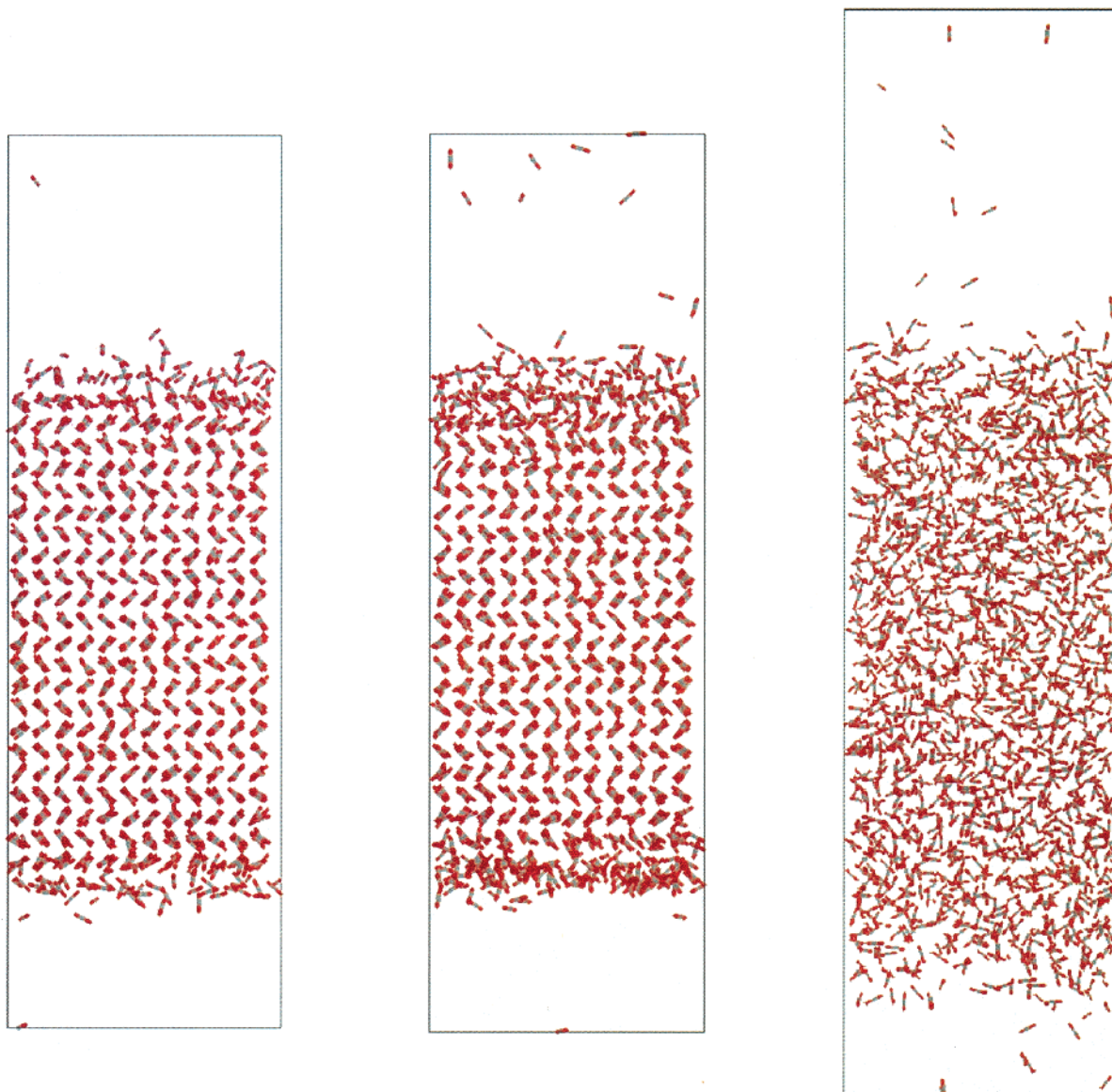


Figure 11. Snapshots of the carbon dioxide slabs at $T = 190$ K (left), 210 K (middle), and 220 K (right).

increase of the order parameter at the solid–vapor (and also liquid–vapor) interface is an artifact arising from the different number of nearest neighbors for interfacial particles. Increasing the temperature leads to a dramatic increase in the width of liquid-like region of the slab and to a lesser increase in the width of the order–disorder interfacial region. The order parameter distributions are shown in Figure 7. Only the solid-like peak is present at $T^* = 0.585$, while the distributions become bimodal as the triple point is approached. It should be emphasized here that the order parameter distributions are only pertinent to the system geometry used here; i.e., the fraction of solid-like material will increase with increasing slab width. However, the width of the liquid-like region should be independent of the system geometry (if sufficiently large slabs are used).

B. Carbon Dioxide. The sublimation and vaporization pressure lines calculated for carbon dioxide and their experimental counterparts⁴⁷ are shown in Figure 8. Agreement for the vapor pressures is excellent over the entire temperature range, while the sublimation pressure is slightly overestimated. It is very encouraging to see that the relatively simple, non-polarizable TraPPE force field for carbon dioxide that was developed by fitting to high-temperature vapor–liquid equilibria

($T > 250$ K)³⁹ can also be applied to low-temperature vapor–liquid equilibria and to solid–vapor equilibria. Nevertheless, it should be pointed out that our earlier grand canonical ensemble simulations³⁹ made use of a site-site truncation at 10 Å and analytical tail corrections for the Lennard–Jones interactions and an Ewald sum with tin-foil boundary conditions for the Coulombic interactions. Thus, the present simulations benefit from a fortuitous error cancellation because the neglect of the analytical tail corrections should lead to an increase in the vapor pressure (see section 4.A), whereas use of a molecule-based cutoff for the charge–charge interactions should cause a decrease in the vapor pressure. As observed for Lennard–Jonesium, the conventional Gibbs ensemble simulations could be extended into the supercooled regime, while the solid-phase melted above the triple point in the solid-slab Gibbs ensemble simulations.

The triple-point properties of carbon dioxide are listed in Table 2. Our simulations yield $T = 212 \pm 2$ K and $p = 430 \pm 50$ kPa. These values are slightly below their experimental counterparts (216.6 K and 518 kPa, respectively^{46–48}) because of the overestimation of the sublimation pressure. The ratios of the triple point over critical point parameters calculated for the TraPPE model and measured experimentally⁴⁷ are as follows:

TABLE 2: Thermodynamic Properties of Carbon Dioxide at Its Triple Point (TP) and Vapor–Liquid (VL) and Solid–Vapor (SV) Coexistence Data near the Triple Point^a

		T [K]	p [MPa]	ρ_{solid} [g/mL]	ρ_{liquid} [g/mL]	ρ_{vapor} [mg/mL]	U_{solid} [kJ/mol]	U_{liquid} [kJ/mol]	U_{vapor} [J/mol]
experiment	TP	216.6	0.518	1.512	1.179	13.8			
this work	TP	212 ₂	0.43 ₅	1.498 ₇	1.182 ₈	11.5 _{1,5}			
this work	VL	220	0.620 ₂₀		1.153 ₁	16.2 ₆		−14.2 ₁	−0.34 ₂
this work	SV	210	0.385 ₇	1.498 ₂		10.3 ₂	−22.8 ₁		−0.23 ₁

^a Subscripts denote the statistical uncertainties in the last digits.

$T_{\text{triple}}^{\text{sim}}/T_{\text{crit}}^{\text{sim}} = 0.691$, $p_{\text{triple}}^{\text{sim}}/p_{\text{crit}}^{\text{sim}} = 0.0546$, $T_{\text{triple}}^{\text{exp}}/T_{\text{crit}}^{\text{exp}} = 0.712$, and $p_{\text{triple}}^{\text{exp}}/p_{\text{crit}}^{\text{exp}} = 0.0702$. The overall agreement is very satisfactory and the three-site TraPPE force field is able to capture the significant difference in these ratios between carbon dioxide and argon (or Lennard-Jonesium).

The heats of sublimation⁴¹ and of vaporization calculated directly from the Gibbs ensemble simulations and obtained from the Clausius–Clapeyron fits are shown in Figure 9. Agreement with the experimental data^{46–48} is very satisfactory. Compared to Lennard–Jonesium, the temperature dependence of the heat of vaporization is more pronounced because carbon dioxide is at a higher reduced temperature. For carbon dioxide, the heat of sublimation at the triple point is about 50% larger in magnitude than the heat of vaporization, i.e., a much bigger jump than for Lennard–Jonesium.

The temperature–density phase diagram of carbon dioxide is shown in Figure 10. The orthobaric liquid and solid densities obtained from the Gibbs ensemble simulations are slightly smaller than the experimental values.^{46–48} In addition, there is very small but noticeable difference between the results of the Gibbs ensemble and grand canonical ensemble simulations which might be attributed to the difference in the treatment of the long-range parts of the Lennard–Jones and Coulomb potentials. More important is the fact, that the simulations properly reproduce the large density (about 26%) increase upon solidification compared to Lennard–Jonesium (13%).

Snapshots of the final configurations of the solid-slab Gibbs ensemble simulations at temperatures below, close, and above the triple point are shown in Figure 11. These snapshots give a first impression of the surface-induced melting transition as the triple-point temperature is exceeded. At $T = 190$ K, only the outermost layer of the solid slab shows significant disorder, while a liquid-like surface film with a depth of about two layers is observed at $T = 210$ K. The translational order parameters determined from the solid slab and the conventional Gibbs ensemble simulations are plotted as a function of z -position in Figure 12, and the corresponding order parameter distributions are shown in Figure 13. In general, the behavior of the translational order parameter appears to be very similar for carbon dioxide and Lennard–Jonesium, as one might expect because both are fcc structures. At $T = 190$ K, the solid slab is highly ordered, and the solid–vapor interface is sharp. At $T = 210$ K, the distribution of order parameters becomes bimodal, and a liquid-like film separates the solid and vapor phases.

While the translational order parameter is sufficient to monitor the solid–fluid transition of Lennard–Jonesium, the orientational order is equally important for molecular systems. The crystal structure of carbon dioxide is of the $Pa3$ type, and the quadrupolar molecules arrange in an approximately T-shaped pattern. The average azimuthal angles of carbon dioxide molecules with the (1,1,1) axis as a function of z -position, and their distribution are plotted in Figures 14 and 15. At $T = 190$ K, the 12 unit cells of the initial solid slab are well preserved. The oscillating pattern along the z -axis and the bimodal

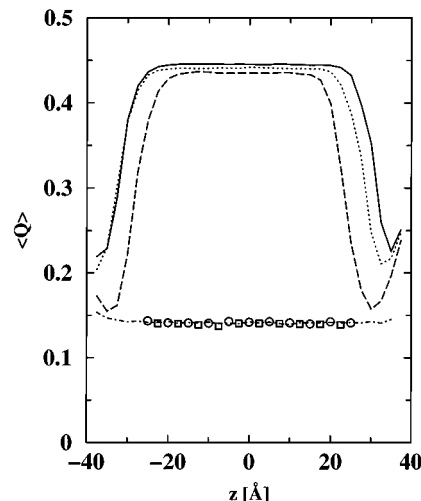


Figure 12. Center-of-mass translational order parameters (eq 1) for carbon dioxide as a function of position along the z -axis. Results for the solid-slab setup (including all regions with density larger than $10^{-2}\rho_{\text{solid}}$) are shown for $T = 190$ K (solid line), $T = 200$ K (dotted), $T = 210$ K (dashed), and $T = 220$ K (dashed-dotted). Results for the bulk liquid are shown for $T = 200$ K (squares) and $T = 220$ K (circles).

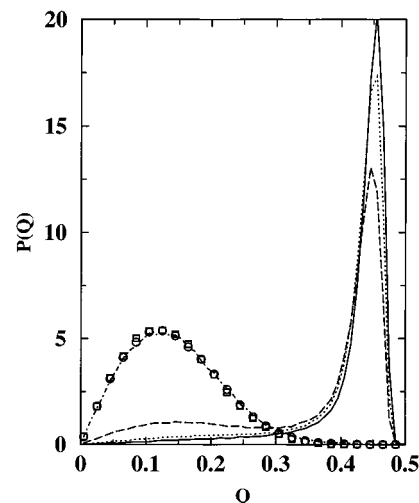


Figure 13. Distributions of center-of-mass translational order parameters (eq 1) for carbon dioxide. Line styles and symbols as in Figure 12.

distribution are caused by the different orientations found in the molecular crystal (see also Figure 11). The carbon dioxide molecules orient along the four body diagonals; thus, we should preferentially observe two angles with the reference (1,1,1) axis—i.e., one-quarter of the molecules aligns with the reference axis, and the other three-quarters align along the other three body diagonals with $\Phi \approx 70^\circ$ ($\cos \Phi \approx 0.33$) (compare also to the integrals under the two peaks in Figure 15). The oscillating z -profiles in Figure 14 reflect the crystal structure where in one layer all molecules are at $\Phi \approx 70^\circ$ and in the next layer half of the molecules are at $\Phi \approx 0^\circ$ and the other half at $\Phi \approx 70^\circ$.

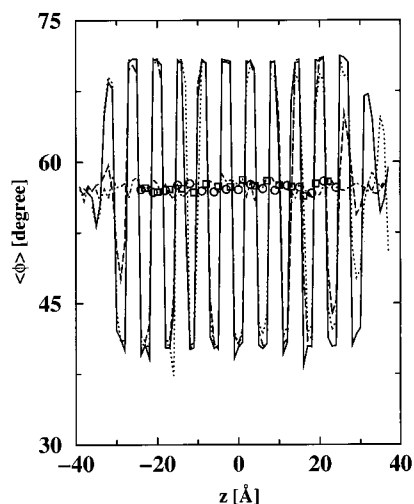


Figure 14. Azimuthal angles for carbon dioxide as a function of position along the z -axis. Solid, dotted, dashed, and dashed-dotted lines as in Figure 12.

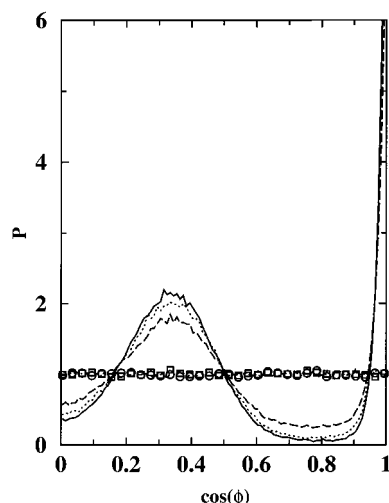


Figure 15. Distributions of azimuthal angles for carbon dioxide. Line styles and symbols as in Figure 12.

Close to the triple point, the liquid-like surface film surrounding the crystalline central region shows greatly reduced orientational order.

The mutual orientations of the long axes of neighboring carbon dioxide molecules (with center-of-mass separations smaller than 5 Å) are shown in Figure 16. In the solid phase, there is a strong preference for T-shaped configurations with a maximum close to 70° in agreement with the tetrahedral arrangement (180–109.5°) found for the experimental crystal structure.^{46–48} Some residual orientational order is present in the bulk liquid phase at $T = 220$ K. The almost complete loss of orientational order of carbon dioxide at the solid–liquid–phase transition is responsible for the large differences between the heats of sublimation and of vaporization (and internal energies, see Table 2) and between the solid and liquid densities. These differences, in turn, are responsible for the unusually high reduced triple-point temperature and pressure found for carbon dioxide compared to argon (while a loss of orientational order by itself would lead to a decrease in the triple-point temperature).

5. Conclusions

An extension to the Gibbs ensemble Monte Carlo method^{1–3} is presented that allows the direct simulation of solid–vapor

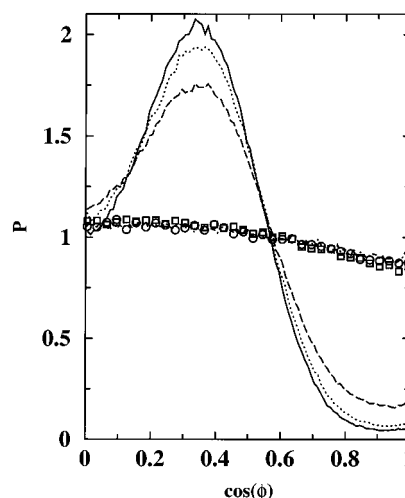


Figure 16. Distributions of mutual orientations for neighboring carbon dioxide molecules. Line styles and symbols as in Figure 12.

phase equilibria. In particular, an elongated box containing a solid slab surrounded by vapor is used for one of the simulation boxes, and configurational-bias Monte Carlo moves and aggregation-volume-bias Monte Carlo moves allow for particle swaps between different simulation boxes and for particle transfer between the solid slab and surrounding vapor. Conventional Gibbs ensemble Monte Carlo simulations cannot be applied to crystalline phases because of the failure to achieve particle insertions/removals, and molecular dynamics simulations of solid–vapor interfacial systems are difficult because transfers from the solid to the vapor are very infrequent and because it is problematic to thermalize the particles after leaving the solid slab on one side and before re-entering at the other side via the periodic boundary conditions.

In its current form, the novel simulation technique requires the presence of one low-density phase to facilitate the enthalpy–entropy balance that is exploited in configurational-bias Monte Carlo particle swaps between solid-slab and vapor boxes and in aggregation-volume-bias Monte Carlo moves within the solid-slab box. Thus, the solid-slab Gibbs ensemble method can be directly applied to solid–liquid–vapor or solid–solid–vapor equilibria but would not work as well for solid–liquid equilibria. However, once the triple point has been located from simulations of solid–vapor and vapor–liquid equilibria, it is straightforward to trace the melting point line using the Gibbs–Duhem integration technique.^{16–18} Since the configurational-bias Monte Carlo moves can also be used to sample internal degrees of freedom, the solid-slab Gibbs ensemble method can be applied without modifications to flexible molecules.

Simulations were carried out to determine the solid–vapor and vapor–liquid coexistence curves of Lennard–Jonesium and of carbon dioxide using the TraPPE force field. Agreement with previous simulation results for Lennard–Jonesium and with experimental data for carbon dioxide is very satisfactory. The unusually high triple-point temperature of carbon dioxide is well reproduced and is attributed to the substantially higher density and more favorable cohesive energy (larger heat of sublimation) of the crystalline form. The orientational order of carbon dioxide is almost completely lost upon liquefaction.

Acknowledgment. We would like to thank James Rainwater and Erich Müller for stimulating talks at the AIChE 2000 Annual Meeting and Jeff Potoff for carrying out the histogram-reweighting grand canonical ensemble simulations for Lennard–Jonesium. Financial support from the National Science Foun-

ation (CTS-9813601), a Sloan Research Fellowship, and a Doctoral Dissertation Fellowship (B.C.) is gratefully acknowledged. Part of the computer resources were provided by the Minnesota Supercomputing Institute.

References and Notes

- (1) Panagiotopoulos, A. Z. *Mol. Phys.* **1987**, *61*, 813.
- (2) Panagiotopoulos, A. Z.; Quirke, N.; Stapleton, M.; Tildesley, D. J. *Mol. Phys.* **1988**, *63*, 527.
- (3) Smit, B.; de Smedt, P.; Frenkel, D. *Mol. Phys.* **1989**, *68*, 931.
- (4) Frenkel, D.; Smit, B. *Understanding Molecular Simulation*; Academic Press: New York, 1996.
- (5) Siepmann, J. I.; Karaborni, S.; Smit, B. *Nature* **1993**, *365*, 330.
- (6) Siepmann, J. I. *Adv. Chem. Phys.* **1999**, *105*, 443.
- (7) Lopez, J. N. C.; Tildesley, D. J. *Mol. Phys.* **1997**, *92*, 187.
- (8) Neubauer, B.; Tavittian, B.; Boutin, A.; Ungerer, P. *Fluid Phase Equilib.* **1999**, *161*, 45.
- (9) Frenkel, D.; McTague, J. P. *Annu. Rev. Phys. Chem.* **1980**, *31*, 491.
- (10) Frenkel, D.; Ladd, A. J. C. *J. Chem. Phys.* **1984**, *81*, 3188.
- (11) Kuchta, B.; Etters, R. D. *Phys. Rev. B* **1993**, *47*, 14691.
- (12) Malanoski, A. P.; Monson, P. A. *J. Chem. Phys.* **1997**, *107*, 6899.
- (13) Polson, J. M.; Frenkel, D. *J. Chem. Phys.* **1998**, *109*, 318.
- (14) Malanoski, A. P.; Monson, P. A. *J. Chem. Phys.* **1999**, *110*, 664.
- (15) Polson, J. M.; Frenkel, D. *J. Chem. Phys.* **1998**, *111*, 1501.
- (16) Kofke, D. A. *Mol. Phys.* **1993**, *78*, 1331.
- (17) Agrawal, R.; Kofke, D. A. *Mol. Phys.* **1995**, *85*, 43.
- (18) Kofke, D. A. *Adv. Chem. Phys.* **1999**, *105*, 405.
- (19) Hoover, W. G.; Ree, F. H. *J. Chem. Phys.* **1968**, *49*, 3609.
- (20) Paras, E. P. A.; Vega, C.; Monson, P. A. *Mol. Phys.* **1993**, *80*, 1063.
- (21) Gay, S. C.; Rainwater, J. C.; Beale, P. D. *J. Chem. Phys.* **2000**, *112*, 9841.
- (22) Siepmann, J. I.; Frenkel, D. *Mol. Phys.* **1992**, *75*, 59.
- (23) Frenkel, D.; Mooij, G. C. A. M.; Smit, B. *J. Phys.: Condens. Matter* **1992**, *4*, 3053.
- (24) Martin, M. G.; Siepmann, J. I. *J. Phys. Chem.* **1999**, *103*, 4508.
- (25) Chen, B.; Siepmann, J. I. *J. Phys. Chem. B* **2000**, *104*, 8725.
- (26) Chen, B.; Siepmann, J. I. *J. Phys. Chem. B*, in press.
- (27) Alejandre, J.; Tildesley, D. J.; Chapela, G. A. *Mol. Phys.* **1995**, *85*, 651.
- (28) Rivera, J. L.; Alejandre, J. *Mol. Phys.* **2001**, in press.
- (29) Gelb, L. D.; Suarez, M. E.; Müller, E. A. *AIChE Symp. Ser.* **2001**, *97*, 187.
- (30) van der Veen, J. F. *Surface Sci.* **1999**, *433–435*, 1.
- (31) Huitema, H. E. A.; Vlot, M. J.; van der Eerden, J. P. *J. Chem. Phys.* **1999**, *111*, 4714.
- (32) For obvious reasons, one should not use individual sampling of cell lengths or **H**-matrix elements for simulations of liquid slabs. In this case, the system will succeed to lower its free energy by shrinking the vapor–liquid interfacial area. The symmetry of the crystalline phase prevents a similar problem for the solid-slab simulations.
- (33) Parrinello, M.; Rahman, A. *Phys. Rev. Lett.* **1980**, *45*, 1196.
- (34) Yashoneth, S.; Rao, C. N. R. *Mol. Phys.* **1985**, *54*, 245.
- (35) Allen, M. P.; Tildesley, D. J. *Computer Simulations of Liquids*; Oxford University Press: Oxford, 1987.
- (36) Vlugt, T. J. H.; Martin, M. G.; Smit, B.; Siepmann, J. I.; Krishna, R. *Mol. Phys.* **1998**, *94*, 727.
- (37) Esselink, K.; Loyens, L. D. J. C.; Smit, B. *Phys. Rev. E* **1995**, *51*, 1560.
- (38) Mackie, A. D.; Tavittian, B.; Boutin, A.; Fuchs, A. H. *Mol. Simul.* **1997**, *19*, 1.
- (39) Potoff, J. J.; Siepmann, J. I. *AIChE J.* **2001**, *47*, 1676.
- (40) Castellan, G. W. *Physical Chemistry*, 3rd ed.; Benjamin/Cummings Publishing: Menlo Park, CA, 1983.
- (41) The internal energy and density of the solid phase were calculated by averaging only over the central region of the solid slab.
- (42) Potoff, J. J. Unpublished results, 2001.
- (43) Wilding, N. B. *Phys. Rev. E* **1995**, *52*, 602.
- (44) Stead, K.; Williams, J. M. J. *J. Chem. Soc., Faraday Trans. 2* **1980**, *76*, 1045.
- (45) van Duijneveldt, J. S.; Frenkel, D. *J. Chem. Phys.* **1992**, *96*, 4655.
- (46) Lide, D. A. *CRC Handbook of Chemistry and Physics*; CRC Press: Boca Raton, FL, 1991.
- (47) Lemmon, E. W.; McLinden, M. O.; Friend, D. G. Thermophysical Properties of Fluid Systems. In *NIST Chemistry WebBook*; NIST Standard Reference Database Number 69; Mallard, W. G., Linstrom, P. J., Eds.; National Institute of Standards and Technology: Gaithersburg, MD, 2000 (<http://webbook.nist.gov>).
- (48) Beilstein CrossFire Database (<http://beilstein.library.wisc.edu>, accessed 2001).